Geophys. J. Int. (2001) **145,** 97–111

Numerical modelling of tsunami generation and propagation from submarine slumps: the 1998 Papua New Guinea event

Ph. Heinrich, A. Piatanesi and H. Hébert

Laboratoire de Détection et de Géophysique, Commissariat à l'Energie Atomique, BP12, 91680 *Bruyères-le-Châtel, France.*
E-mail: heinrich@dase.bruyeres.cea.fr

Accepted 2000 September 20. Received 2000 September 20; in original form 2000 February 17

SUMMARY

Deep and large submarine slumps may generate tsunamis as disastrous as tsunamis of tectonic origin. Such a landslide is likely to be the origin of the 1998 July 17 tsunami of Papua New Guinea, the deadliest tsunami in the last 50 years. Water waves devastated a 20 km stretch of coastline, wiping out three villages and killing more than 2200 people. A numerical model has been developed to study the efficiency of deep slumps in producing tsunamis and has been applied to the Papua New Guinea event.

The landslide is treated as the flow of a homogeneous gravity-driven continuum governed by a rheological law. Water waves are generated by sea-bottom displacements induced by the landslide. The shallow-water approximation is adopted for both the landslide and the associated water waves. The resulting differential equations are solved by a finite difference method based on shock-capturing. The shallow-water hypothesis is tested by comparison with a model solving Navier–Stokes equations for a mixture of water and sediments. Sensitivity tests carried out for a 2-D simplified geometry show that the water surface profile depends strongly on the constitutive law of the landslide.

The 1998 event is simulated numerically by the shallow-water model, testing different friction laws. The observed inundation height distribution is well reproduced by the model for a volume of 4 km^3, with its top located at a water depth of 550 m, and sliding with a Coulomb-type friction law over a distance of 5 km.

Key words: granular flows, numerical modelling, shallow water, submarine landslides, tsunami.

1 INTRODUCTION

Recent bathymetric and seismic reflection surveys have revealed that submarine landslides are abundant on the seafloor but most of them occurred unobserved or in prehistoric times (Hampton *et al.* 1996). The largest ones are generally discovered since they produce tsunamis that may devastate a coastal segment, or that erode marine and coastal sediments and deposit them far away inland. The best example illustrating this phenomenon is described by Moore *et al.* (1989) for giant submarine landslides on the flanks of the Hawaiian islands, where tsunami deposits have been found at elevations as high as 300 m.

In July 1998, a relatively modest earthquake ($M_s = 7.0$) in northern Papua New Guinea (PNG) generated a tsunami that devastated unexpectedly a 20 km stretch of coastline, with inundation heights close to 10 m. The seismic event belongs to the category of 'tsunami earthquakes', since it excites considerably larger tsunami than expected from seismic waves (Kanamori 1972). Two types of tsunami earthquakes may be distinguished: those occurring in subduction zones, with a slow and long rupture, and those triggering occasional slumping. On the basis of recorded seismic waves (Newman & Okal 1998), the first type may be ruled out; the origin of the tsunami was attributed very early on to a submarine slump (Tappin *et al.* 1999a; Kawata *et al.* 1999a), which was confirmed later by bathymetric and seismic reflection surveys.

Depending on the material properties, three types of landslides may be distinguished: slumps, debris avalanches and debris flows. Slumps consist of relatively undisturbed masses, travelling a short distance along the rupture plane (Moore *et al.* 1989). Debris avalanches consist of rocks and sediments broken into numerous discrete blocks, moving very large run-out distances. Debris flows are composed of water-saturated unlithified sediments (Iverson 1997) that may evolve after water inclusion into turbidity currents travelling very large distances (several hundreds of kilometres). According to marine surveys, the 1998 event was a submarine slump composed of cohesive sediments and bedrock, sliding a few kilometres without large disturbances.

The modelling of water waves generated by landslides (Sander & Hutter 1996) is still poorly understood and is generally based on two major assumptions. The first concerns the generation mechanism and the second the equations governing the water and landslide motion. Most of the numerical models simulate the generation mechanism as the prescribed motion of the fluid domain boundaries. For instance, landslides are modelled by submerged or partly emerging pistons (Sander & Hutter 1992, 1996), by a rigid triangular box impacting the water mass (Heinrich 1992), by a submarine rectangular box (Harbitz 1992) or by an initial upward water displacement corresponding to the volume of a landslide entering the sea (Nomanbhoy & Satake 1995). Recently, some authors have developed models calculating landslide kinetics. Tinti *et al.* (1997, 1999) considered the landslide mass as a chain of contiguous blocks subjected to mutual interaction and external forces and calculated the landslide kinetics based on a Lagrangian point of view. Fine *et al.* (1999) extended in three dimensions the shallow-water model developed by Jiang & Leblond (1992, 1993), which considers the landslide as a viscous flow and deals with the interaction between water waves and the landslide, both modelled on the basis of the shallow-water assumption. A similar model has been developed and is presented in this paper. The major difference is the possibility of dealing with non-Newtonian constitutive laws for the landslide. The action of water waves on the landslide, however, has not been taken into account, since it is negligible for deep landslides (Jiang & Leblond 1992). The sea-bottom deformation induced by the landslide is used as input data in the tsunami model.

The second approximation concerns the shallow-water hypothesis. Landslides and water waves are generally modelled on the basis of the shallow-water assumption. We propose to test this assumption, by comparing our shallow-water model with a Navier–Stokes model developed for a mixture of two fluids (Assier *et al.* 1997). This latter model deals with the full interaction of landslide and water, including the deformation of the mass.

In the first part of this paper, the recent event that occurred off the PNG coast on 1998 July 17 is described from the available literature on this subject. The next paragraphs are devoted to the numerical simulation of landslide-generated water waves with application to PNG. First, 1-D preliminary tests for a simplified geometry are carried out to test the shallow-water model by comparison with a model solving Navier–Stokes equations for a mixture of two fluids. Next, simulations based on the shallow-water approach allow one to study the influence of the constitutive law that governs the landslide velocity and therefore controls the tsunami generation. Sensitivity tests for a simplified geometry are investigated by testing different constitutive laws and varying the associated parameters. Finally, the 2-D simulation of the 1998 event is carried out using either viscous laws or Coulomb-type friction laws, with coefficients in the range investigated by 1-D tests. The analysis of 1-D and 2-D numerical results allows us to understand better the generation mechanism of deep landslides.

2 DESCRIPTION OF THE 1998 JULY 17 EVENT

On 1998 July 17, an earthquake of magnitude ($M_s = 7$) occurred in the Sandaun province of Papua New Guinea and was followed 20 min later by a catastrophic tsunami, causing the destruction of several villages and the loss of 2200 lives. The devastated area was the subject of a detailed survey by an international team who mapped the inundation by measuring 80 inundation heights along a coastal segment of 40 km (Kawata *et al.* 1999a,b). The maximum run-up heights reach 15 m at the centre of the affected area, i.e. at Sissano lagoon. Unusual features of this tsunami are the exceptionally large water heights given the size of the earthquake and its strong concentration along the coast, with run-up heights decreasing rapidly to 4 m only 15 km away from Sissano (Okal 1999a). The offshore surveys were carried out by the Japan Marine Science and Technology Center (JAMSTEC) and the South Pacific Applied Geoscience Commission (SOPAC). The bathymetry that we have built (Fig. 1) uses the data from these surveys for depths greater than 200 m and data from nautical charts for shallower depths. It is characterized by a narrow shelf area (10 km wide) and a steep continental slope (about 10°) leading to a trench at 4000 m water depth (Matsuyama *et al.* 1999).

The tsunami generation mechanism is still controversial and several researchers have attributed it to the earthquake. Iwabuchi *et al.* (2000) noted that no recent turbidites were recognized from piston core samples on the lobe of the presumed landslide, and that the geomorphological features of this landslide are not recent. Moreover, Tanioka (1999) showed that the far-field tsunami signals in Japan are compatible with the earthquake source, without any additional tsunami source such as a sediment slump. The main objection is that a landslide is essentially a dipolar source, and hence a deficient far-field generator. Far-field tsunami propagation is affected by frequency dispersion and far-field data cannot resolve a landslide source. In the near field, numerical simulations of tsunami propagation were carried out by Matsuyama *et al.* (1999) showing that new bathymetric data concentrate energy in the Sissano region. They suggested, following Titov & Gonzalez (1998, 2000), a steep reverse fault as the earthquake mechanism, and concluded that this earthquake could be the tsunamigenic source. However, there are several arguments against this hypothesis.

(1) The analysis of seismic data and in particular of the widely scattered distribution of aftershocks is in favour of a conjugate fault mechanism, that is, a classic low-angle thrust subduction (Kikuchi *et al.* 1998; Okal *et al.* 1999a; Heinrich *et al.* 2000).

(2) Whatever the fault plane we choose, the values of the observed run-up heights require an increase in the simulation of the dislocation slip estimated from seismic data by a factor larger than 10 (Heinrich *et al.* 2000), which is inconsistent with the seismic moment.

(3) The timing of the tsunami indicates that the coast was affected about 20 min after the main shock (Tappin *et al.* 1999a), whereas the traveltime of water waves is only about 10 min from a source located at epicentres estimated from seismic data, that is, 20 km offshore away from Sissano. The 10 min hiatus could be accounted for by a time delay between the main shock and the landslide triggering. An aftershock did take place 13 min after the main shock but its magnitude was too small, $m_b = 4.4$, for its dislocation to be the tsunami source. It could be objected that locals might have a poor perception of absolute time during an emergency situation. However, the tsunami timing, established during interviews by members of

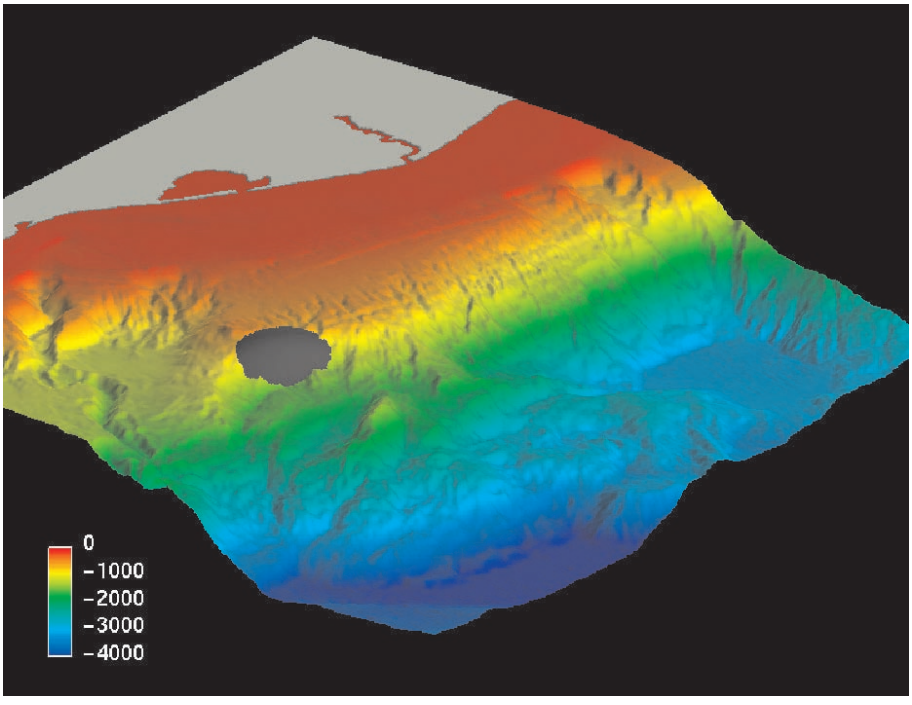

Figure 1. 3-D view of the bathymetry off the Papua New Guinea coasts. The landslide volume is defined as the intersection of an ellipsoidal volume with the existing bathymetry and covers approximately an area of 5 km by 3 km, with a maximum thickness of 450 m. The volume is located at water depths between 550 and 1500 m on a 15° slope. The horizontal dimensions of the domain are 55 km by 55 km.

the post-tsunami survey team (Kawata *et al.* 1999a,b), was based on the relative time differences of the main aftershock (about 20 min after the main shock) and the tsunami.

(4) The aftershock with $m_b = 4.4$ generated acoustic T waves recorded at Wake Island (Okal 1999b), lasting close to 1 min, an abnormally long duration for a small seismic shock, which suggests that this event might be a landslide rather than a seismic dislocation.

(5) Two oceanographic surveys were carried out in 1999 and confirmed evidence of a large submarine slump in a depression with an area of 50 km^2 located 20 km offshore (Tappin *et al.* 1999a), whereas major reverse faulting was not observed in this region. Within the depression, seabed imaging by a remotely operated vehicle indicated a recent landslide, in the form of fissures, brecciated sediment and fresh rock talus deposits (Tappin *et al.* 1999b). Seismic reflection surveys show the internal structure of a rotational slump, with a volume of several kilometres cubed, some hundreds of metres thick (Tappin *et al.* 1999b; Sweet *et al.* 1999). The landslide slid a few kilometres away from its initial presumed position and halted as the toe came to lie on a flat area (Fig. 1) at a mean water depth of 2000 m. Of course, this survey proves only that a slide has occurred in the past, but in the absence of pre-event bathymetry, there is no indication when it occurred exactly.

3 A SHALLOW-WATER MODEL FOR SIMULATING LANDSLIDES AND ASSOCIATED WATER WAVES

This paper is focused on landslide and tsunami simulations based on the shallow-water (SW) approximation. The Navier–Stokes (NS) model, mentioned in the Introduction, is described briefly in the Appendix.

3.1 Description of the landslide model

The mechanism initiating the landslide is not investigated in this study and it is assumed that the whole mass suddenly loses its equilibrium and begins to flow down the slope. The landslide is treated as an incompressible homogeneous gravity-driven continuum submitted to buoyancy and internal and basal friction. The 1998 landslide is described as a slump travelling a short distance (Tappin *et al.* 1999a), in which the presence of water probably plays a minor role. Interfacial mixing with water is thus not dealt with and hydrodynamic drag forces are assumed to be negligible compared to basal friction.

Two models for the landslide are considered in this study. The first, well suited to muddy debris flows, considers a landslide as the flow of a viscous fluid. This model is the most commonly used for submarine landslides (Jiang & Leblond 1992; Fine *et al.* 1999; Rabinovich *et al.* 1999) but may also reproduce the behaviour of subaerial landslides (Sousa & Voight 1991, 1995; McEwen & Malin 1989). Viscous flows are associated with parabolic profile of the horizontal velocity, vanishing at the seabed. The shear stress is linearly related to the shear rate through the viscosity coefficient.

The second model assumes that the landslide breaks into fragments during the early stages of collapse (Kilburn & Sorensen 1998) and that it may be assimilated in a fluid-like flow of cohesionless granular material (Savage & Hutter 1989). Although large deformations throughout the thickness are inevitable, most fragment collisions and deformations are assumed to be concentrated in the boundary layer near the bed surface. This hypothesis is consistent with the preservation of pre-failure stratigraphy observed in deposits of debris avalanches. Energy dissipation within the flow is then neglected compared to that lost through the boundary layer, and the

slope-parallel velocity is assumed to be constant over the flow thickness. For simplicity, basal friction is modelled in this study by a Coulomb-type friction law with a constant friction angle, independent of the shear rate. This hypothesis may be criticized, since laboratory experiments on granular flows show a dependence of this angle on the Froude number (Savage & Hutter 1991; Pouliquen 1999). Moreover, Kilburn & Sorensen (1998) and Dade & Huppert (1998) suggested that the basal layer obeys a collisional regime, where the shear stress is proportional to the square of the velocity (Bagnold 1954).

For both landslide models, the associated water waves are calculated by solving SW equations. Sea bottom deformation induced by the landslide is introduced in the mass conservation equation of the tsunami model. The action of water waves on the landslides is neglected since the landslide is deep and amplitudes of water waves are small compared to the water depth (Jiang & Leblond 1992). Moreover, water waves in the offshore direction travel much faster than the landslide, so that they propagate without any interaction as soon as they leave the generation area.

3.2 Governing equations for the water waves and the landslide

The SW approximation is used for both the water waves and the landslide. This implies that the characteristic lengths of water waves are much larger than the water depth and that the slide thickness is much smaller than the length and width of the slide. For both media, depth-averaging over the water depth or over the slide thickness is performed, assuming hydrostatic pressure.

3.2.1 *Shallow-water model for water waves*

The non-linear SW equations we solve are referred to as $2+1$ in the literature (Titov & Synolakis 1998), indicating that there are two spatial horizontal propagation directions (x and y) and one temporal direction (t). Hereafter, the term 1-D is used for $(1+1)$ simulations and the term 2-D for $(2+1)$ simulations in a 3-D geometry. Depth-averaging the equations of mass and momentum conservation leads to evolution equations for h, (hu) and (hv), where h is the water layer thickness and $\mathbf{u}=(u, v)$ is the depth-averaged horizontal velocity. In a conservative form, these equations read

$$\frac{\partial h}{\partial t}+\frac{\partial}{\partial x}(hu)+\frac{\partial}{\partial y}(hv)=0 \quad \text{(mass conservation)}, \tag{1}$$

$$\frac{\partial}{\partial t}(hu)+\frac{\partial}{\partial x}(hu\,u)+\frac{\partial}{\partial y}(hu\,v)=-\frac{1}{2}\frac{\partial}{\partial x}(gh^2)+gh\frac{\partial d}{\partial x}+F_x, \tag{2}$$

$$\frac{\partial}{\partial t}(hv)+\frac{\partial}{\partial x}(hv\,u)+\frac{\partial}{\partial y}(hv\,v)=-\frac{1}{2}\frac{\partial}{\partial y}(gh^2)+gh\frac{\partial d}{\partial y}+F_y$$

$$\text{(momentum conservation)}, \tag{3}$$

where $d(x, y, t)$ is the bathymetry and is related to h by $h(x, y, t)=d(x, y, t)+\eta(x, y, t)$, $\eta(x, y, t)$ being the water surface elevation. F is the friction force on the sea bottom, defined by the Chezy formula. Temporal variations of d induced by the landslide are taken into account in the mass conservation equation.

3.2.2 *Shallowness model for the landslide*

For the slide, mass and momentum conservation equations are depth-averaged over the slide thickness in a similar way to tsunami equations. The precise mechanical behaviour within the flow is then ignored, since the stress distribution throughout the thickness is not considered. Equations are written in a coordinate system linked to the topography (Fig. 2). In this system (x, y) and z denote, respectively, slope-parallel and slope-normal coordinates, $h(x, y, t)$ is the layer thickness perpendicular to the slope and the velocity $\mathbf{u}=(u, v)$ is the depth-averaged velocity parallel to the bed (Savage & Hutter 1989; Hutter 1996). The interface between the water and the mass is assumed to be stress-free, while longitudinal gradients of the deviatoric stress are neglected throughout the flow. The continuity equation (1) is unchanged and the momentum equations read

$$\frac{\partial}{\partial t}(hu)+\alpha\frac{\partial}{\partial x}(hu\,u)+\alpha\frac{\partial}{\partial y}(hu\,v)$$

$$=-\frac{1}{2}\kappa\frac{\partial}{\partial x}(gh^2\cos\theta)+\kappa gh\sin\theta_x-\tau_{xz(z=0)}, \tag{4}$$

$$\frac{\partial}{\partial t}(hv)+\alpha\frac{\partial}{\partial x}(hv\,u)+\alpha\frac{\partial}{\partial y}(hv\,v)$$

$$=-\frac{1}{2}\kappa\frac{\partial}{\partial y}(gh^2\cos\theta)+\kappa gh\sin\theta_y-\tau_{yz(z=0)}, \tag{5}$$

$$\kappa=1-\rho_w/\rho_s, \tag{6}$$

where ρ_w and ρ_s are the water and sediments densities, with a density ratio $\rho_s/\rho_w=2$. Values of α that deviate from unity provide information about the deviation of the slope normal profile of (u, v) from uniformity, $\tau_{xz(z=0)}$ and $\tau_{yz(z=0)}$ are the shear stresses at the bed surface, $\theta(x, y)$ is the local steepest slope angle and θ_x and θ_y are the slope angles along x- and y-axes, respectively.

3.2.3 *Granular flows*

When introducing constitutive laws in depth-averaged equations, it is required to make an *a priori* assumption about the profile of the slope-parallel velocity. Assuming that the deformation is concentrated in a thin boundary layer near the bed surface, the slope-parallel velocity is taken as constant over the thickness (Savage & Hutter 1989). In this case, depth-averaging squared velocities yields $\overline{u^2}=\overline{u}^2$ and $\alpha=1$. This hypothesis is not confirmed by laboratory experiments on dry granular flows, suggesting rather a linear profile for this velocity (Douady *et al.* 1999), which leads to $\alpha=4/3$.

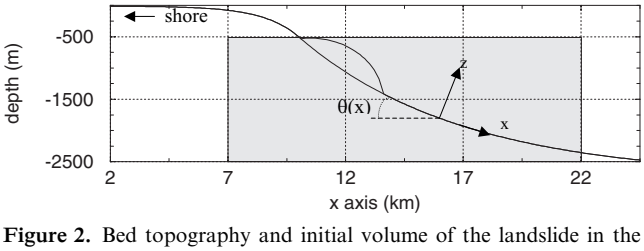

Figure 2. Bed topography and initial volume of the landslide in the topography-linked coordinate system (x, z). $\theta(x)$ is the local slope angle. This simplified geometry is used for 1-D preliminary simulations. The grey area defines the domain of Fig. 7(c).

The constitutive law governing granular flows is generally the Coulomb-type friction law defined in the x-direction by

$$\tau_{xz(z=0)} = \kappa g h \cos\theta \tan\varphi \, \frac{u}{\|\mathbf{u}\|} \,. \tag{7}$$

This law is similar to a friction law for a rigid block on an inclined plane, it assumes a constant ratio of the shear stress to the normal stress at the base and involves a friction angle φ between the rough bed and the mass. When the flow is close to rest, the fluid velocity is set to 0 as soon as the Coulomb force is larger than the algebraic sum of the forces due to gravity and height gradient. Most natural rock types have friction angles between 30° and 45°, so sliding movement should be possible only over areas with an average slope of at least 30°. Nevertheless, it appears that only low values of the friction angle ($<15°$) are appropriate to reproduce the mobility of real landslides. It must also be noticed that dynamic angles are several degrees below the static value (Hutter 1996).

3.2.4 *Viscous flows*

Modelling the landslide as a viscous flow requires a parabolic profile of the slope-parallel velocity, with a no-slip condition at the sea bottom (Jiang & Leblond 1992). In this case, $\alpha = 6/5$ and the shear stress at the sea bottom is

$$\tau_{xz(z=0} = -3\mu u/(h\rho_s) \,, \tag{8}$$

where μ is the dynamic viscosity.

Viscous flows never stop on the sea bottom whatever the viscosity coefficient. An improvement of this model is then to consider the landslide as a Bingham or viscoplastic fluid. No deformation takes place until the shear stress exceeds a threshold value or the Bingham stress. Above the yield stress, the material flows like a viscous fluid. Considering that equations are depth-averaged, the Bingham model requires two systems of equations to be solved, corresponding to two distinct zones in the flow, a shear flow driven by viscosity and a plug flow above it with a uniform velocity profile (Jiang & Leblond 1993). To overcome this difficulty, a simplification consists of considering a single layer whose motion is initiated and driven by viscosity when the shear stress exceeds a given yield stress (Norem *et al.* 1991; McEwen & Malin 1989).

3.3 Numerical scheme

It is worth noting that equations of tsunami propagation are similar to those governing the landslide when written in a conservative form. This similarity allows us to use the same numerical scheme for both media. The numerical model is based on a shock-capturing method and uses a Godunov-type scheme, extended to second order.

Long-wave equations are hyperbolic differential equations admitting discontinuous solutions that correspond to steep fronts (in the case of landslides) or bores (in the case of water waves). These regions are characterized by strong gradients of velocities and flow heights, which classic numerical schemes are not able to treat without producing numerical oscillations. In the case of negligible diffusion terms (such as viscosity) in the momentum equations, artificial viscosities are generally introduced or a filter is used to suppress numerical instabilities in the numerical solution. Recently, several authors have developed numerical models accurately dealing with discontinuities in flow models (Naaim *et al.* 1997; Laigle & Coussot 1997) and in SW models (Titov & Synolakis 1998; Alcrudo & Garcia-Navarro 1993; Fraccarollo & Toro 1995).

The precision and stability of our model have been studied comparing the results with those of an analytical solution for dam-break-type problems (Mangeney *et al.* 2000). The heart of the method is a 1-D Lagrangian scheme, the results of which are remapped onto the desired Euler grid in a separate step. Our method is especially well suited for the treatment of strong discontinuities, accurately dealt with by using shock formulae. Since two dimensions are covered through space splitting, the numerical method will be described only for the 1-D configuration in the x-direction.

Using the Lagrangian approach, eqs (1)–(4) may be expressed as follows:

$$\frac{dV}{dt} = 0 \,, \tag{9}$$

$$h\,\frac{du}{dt} = -\frac{\partial p}{\partial x} + F \,, \tag{10}$$

where V is the volume of the fluid associated with a cell length Δx, $V = h\Delta x$, F denotes the gravity and friction forces, and p, hereafter called 'pressure', is defined as

$$p = \frac{1}{2}\,\kappa g h^2 \cos\theta \qquad \text{(for landslides)}$$

or

$$p = \frac{1}{2}\,g h^2 \qquad \text{(for tsunamis)} \,. \tag{11}$$

Eqs (11) are the analogues of state equations of barotropic compressible fluids, where p and h are the analogues of pressure and density, respectively. The unknowns of the problem u and p are calculated at the cell centres. The numerical scheme of our method consists of four steps. First, a linear Rieman problem is solved to calculate preliminary velocities u^* and pressures p^* at the cell interfaces at time n from cell-centred values using a classic shock formula for compressible fluids, i.e. $\Delta p = \rho c \Delta u$. Values of u^* and p^* are calculated from this shock formula as follows:

$$u^* = \frac{u_l h_l c_l + u_r h_r c_r + p_l - p_r}{h_l c_l + h_r c_r} \,, \tag{12}$$

$$p^* = \frac{p_l h_r c_r + p_r h_l c_l + (u_l - u_r) h_l h_r c_l c_r}{h_l c_l + h_r c_r} \,, \tag{13}$$

where $l = i$ and $r = i+1$ represent, respectively, the left and right cells of the interface and c is the wave celerity defined by $c^2 = gh\cos\theta$ for landslides and $c^2 = gh$ in the tsunami model.

The second step is the application of a Lax–Wendroff scheme, centred and second-order accurate in time and space, in which velocities and pressures are calculated explicitly at time $(n+1/2)$ and at the cell interfaces $(i+1/2)$. In order to suppress numerical oscillations generated by the second-order scheme in space, p and u are determined from values calculated in eqs (12) and (13) in the following way (time discretization is omitted to highlight space discretization):

$$p_{i+1/2} = p^* + \frac{Q}{2}\,(p_{i+1} - p^*) + \frac{Q}{2}\,(p_i - p^*) \,, \tag{14}$$

$$u_{i+1/2} = u^* + \frac{Q}{2}\,(u_{i+1} - u^*) + \frac{Q}{2}\,(u_i - u^*) \,, \tag{15}$$

Slope limiters defined by Q (Harten 1983) are used for both velocity and pressure differences ($p_i - p^*$) and ($u_i - u^*$). The limiter concept allows one to obtain a first-order stable solution for the discontinuities ($Q=0$, equivalent to a Godunov scheme) and a second-order solution elsewhere ($Q=1$, equivalent to a Lax–Wendroff scheme).

The third step consists of solving eqs (9) and (10). First, the displacements of mesh points are calculated using the previous interface velocities at time $(n+1/2)$. New fluid heights in the Lagrangian cells are then inferred from mass conservation (eq. 9). Second, new cell-centred velocities u at time $(n+1)$ are calculated by solving the momentum equation,

$$u_i^{n+1} = u_i^n + \frac{\Delta t}{h_i}\left(-\frac{p_{i+1/2}^{n+1/2} - p_{i-1/2}^{n+1/2}}{\Delta x} + F\right). \quad (16)$$

Finally, a projection of the quantities h and u is carried out on a fixed Eulerian grid. The second order in space is preserved by varying h and u as affine functions across each cell, which corresponds to the concept of Van Leer (1979). The stability of the scheme is obtained with a time step satisfying the CFL (Courant–Friedrichs–Lewy) condition.

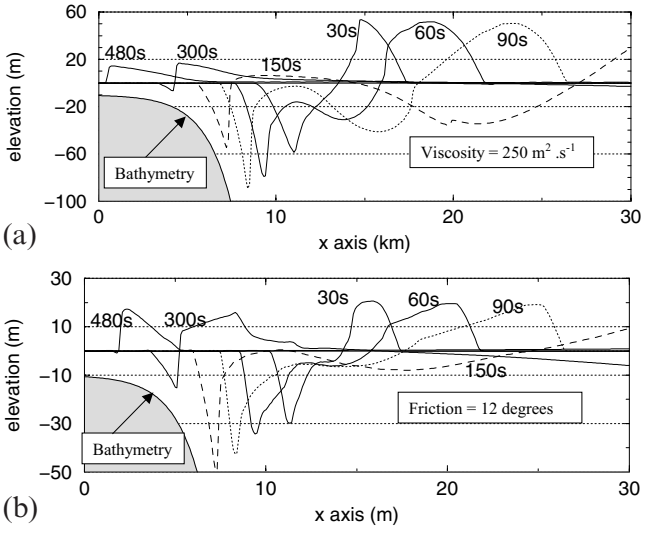

Figure 3. Water elevation profiles calculated at different times for the simplified geometry defined in Fig. 2. (**a**) The landslide is treated as a viscous flow with a kinematic viscosity $v=250$ m^2 s^{-1}. (**b**) The landslide is treated as a granular flow with $\varphi=12^\circ$.

4 PRELIMINARY SIMULATIONS OVER SIMPLIFIED TOPOGRAPHY

Due to the high computational cost of simulations for real events and in order to understand the main mechanisms of water wave generation, preliminary tests are carried out for an approximate vertical profile of the real bathymetry (Fig. 2). Local irregularities of the bathymetry have been removed by simplifying the geometry: the bathymetry consists of one exponential curve with an angle varying from 0° at $x=0$ to 17° at $x=10$ km linked to a second exponential curve with an angle decreasing more slowly from 17° to 0°. The landslide is defined as the intersection of an ellipsoid with the bathymetry. The resulting volume is released from rest at the origin time $t=0$ s.

Waves produced by landslides have typical patterns, shown in Figs 3(a) and (b), where two specific cases corresponding to a viscous flow with a kinematic coefficient $v=250$ m^2 s^{-1} and to a granular flow with $\varphi=12^\circ$ have been taken as illustrative examples. These simulations have been carried out by the SW model using a grid step of 100 m and a time step of 0.2 s.

As for all submarine landslides, water ahead of the front face of the slide is pushed away, creating a positive wave in the slide direction that represents most of the tsunami energy. Above the landslide, water is sucked, which creates a large trough splitting into two waves, one wave propagating shorewards and the other offshore. Later, the shoreward-propagating wave is followed by a positive wave, responsible for coastal inundation and on which attention will be focused.

From a mathematical point of view, the water surface generated may be expressed by analytical methods as a function of the Froude number, defined by the ratio of the landslide speed to the free-wave phase celerity $F_d = V/(gd)^{1/2}$ (Tinti *et al.* 2000; Pelinovsky & Poplavsky 1996). In our case, the flow regime is subcritical, with maximum Froude numbers of 0.2–0.6, the mean water depth being 1000 m for maximum landslide velocities of 20–60 m s^{-1}. Under these circumstances, it can be shown that two main systems of waves (or dipoles), each composed of one trough and one crest, are produced. The first dipole with a leading elevation wave propagates offshore, whereas the second dipole with a leading depression wave propagates shorewards. The first dipole is composed of free progressing waves travelling at $(gd)^{1/2}$ and of a forced trough, with the same profile as the landslide and propagating at the landslide speed.

4.1 Validation of the shallow-water approximation

The SW approximation is tested in this paragraph for both landslides and water waves. To our knowledge, comparisons between SW and NS models are almost absent in the literature due to the complexity of NS models. The NS model, described in the Appendix, deals with the full interaction between sediments and water considered as a mixture of two fluids (Assier *et al.* 1997; Heinrich *et al.* 1998a) and implicitly deals with the propagation of water waves taking into account frequency dispersion.

The first simulations are carried out for an ideal fluid of density 2000 kg m^{-3} without a rheological law and without diffusion. In both models, friction between ambient water and sediments is neglected at the interface and a free-slip condition is applied along the slope. The resulting water surfaces are shown at $t=60$ and 180 s after the landslide initiation in Fig. 4(a). Comparisons between the water surfaces calculated by the SW and NS models show large differences, mainly due to the mass distributions calculated by the models: the mass computed by the NS model is mainly concentrated at the front of the landslide (Fig. 4b). These differences are accounted for by the SW hypothesis, neglecting vertical accelerations. In both models, the front face of the landslide is driven by gravity, buoyancy and pressure forces exerted to the rear of the slide. In the NS model, the slowdown by water induces vertical acceleration inside the sediments and a large deformation in the mass front, which in turn is slowed down by water.

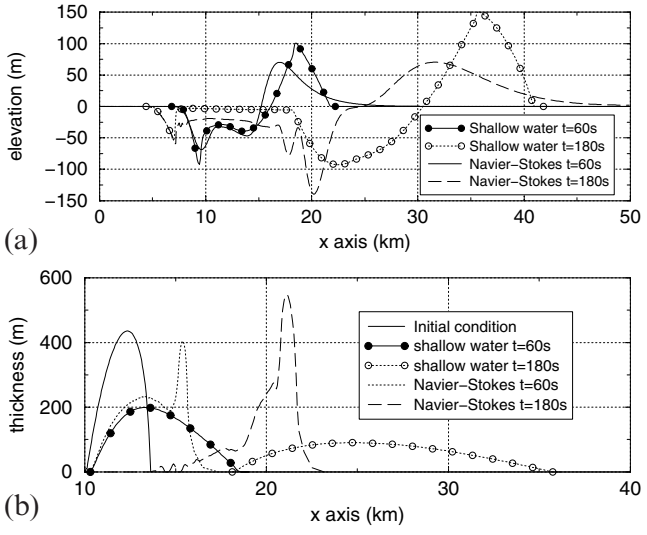

Figure 4. Simulations by NS and SW models for **a** landslide considered as a perfect fluid with a density of 2 and the geometry defined in Fig. 2. (a) Comparisons of water elevation profiles calculated at $t=60$ and 180 s. **(b)** Comparisons of the landslide profiles calculated at $t=60$ and 180 s.

The second comparison is made by considering the landslide as a viscous fluid with a kinematic coefficient $v=250$ m^2 s^{-1}. A no-slip condition is used in the NS model, which is probably the best way of reproducing the prescribed parabolic profile in the SW model. In this case the landslide profiles are similar (Fig. 5b), with a strongly reduced front height in the NS model. As expected, water surfaces are much closer to each other (Fig. 5a), which validates the SW approach in this case. It is worth noting that the second positive wave has already formed at $t=180$ s in the SW simulation and that the filling in of the trough begins later in the NS model owing to non-uniform vertical water velocities.

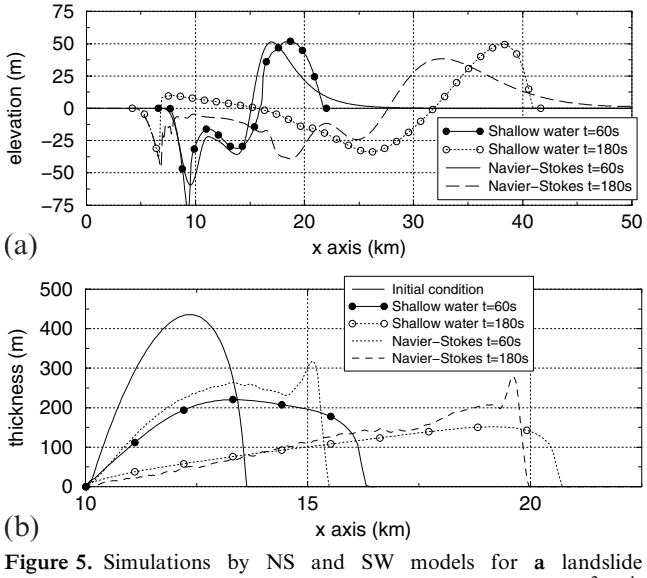

Figure 5. Simulations by NS and SW models for **a** landslide considered as a viscous flow with a kinematic viscosity $v=250$ m^2 s^{-1}. (a) Comparisons of water elevation profiles calculated at $t=60$ and 180 s. **(b)** Comparisons of the landslide profiles calculated at $t=60$ and 180 s.

Due to the complexity of the NS model and its computational cost, the validation of the SW approximation cannot be performed systematically. For short wavelengths, the amplitudes of water waves are expected to be attenuated in the NS model through the water column during tsunami generation. The attenuation factor for the leading wave may be estimated by $\cosh(2\pi d/\lambda)$, where λ is the characteristic wavelength and d is the water depth (Kajiura 1963). Assuming that the water surfaces generated by the viscous flow are representative of the PNG event, Fig. 5(a) shows that at $t=60$ s wavelengths are about 15 km for a mean water depth of 1500 m and that at $t=180$ s wavelengths are about 25 km for a mean water depth of 2500 m. The factor $\cosh(2\pi d/\lambda)$ then ranges from 1.1 to 1.2, which is consistent with the amplitude differences of water waves in Fig. 5(a).

The short wavelengths compared to water depth as well as the steep slopes do not favour the SW approximation. However, water wave characteristics are close enough to conclude that the SW model is valid in the framework of this study.

4.2 Water wave generation by viscous flows

The most common constitutive law used to model submarine landslides is a viscous law (Norem *et al.* 1991). The influence of the viscosity on water wave generation is investigated by varying, for the same geometry, the kinematic viscosity from 25 to 500 m^2 s^{-1}. These values are in the range of calculated and observed subaerial debris avalanches (Sousa & Voight 1991, 1995). The resulting maximum velocities of the landslide vary from 20 to 60 m s^{-1}, reached between 50 and 90 s after landslide initiation.

Fig. 6(a) shows the maximum and minimum calculated water surface elevations in the computed domain, the simulation being stopped shortly after wave reflection against the shoreline.

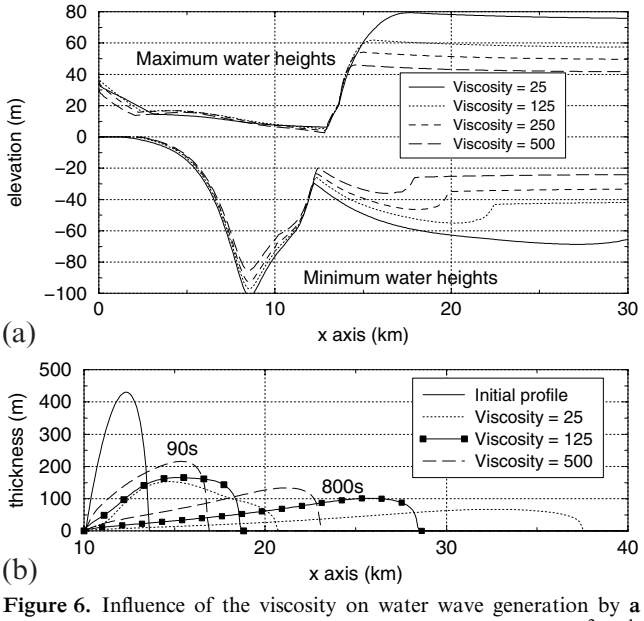

Figure 6. Influence of the viscosity on water wave generation by **a** viscous flow. Kinematic viscosities vary from $v=25$ to 500 m^2 s^{-1}. (a) Maximum and minimum water elevations reached during the tsunami propagation, stopped after reflection against the shoreline. **(b)** Comparisons between landslide profiles at $t=90$ and 800 s.

4.2.1 Interpretation of the minimum and maximum water heights

The representation of Fig. 6(a) shows the main features of tsunami generation by a landslide. The curves of minimum heights show the formation of the main trough at $x=11$ km (at a water depth of about 800 m), its shoreward propagation with amplification from $x=11$ to $x=8.5$ km (at a water depth of 200 m) and later the decrease of the trough from $x=8.5$ km to $x=0$, due to the faster propagation of the second positive wave, catching up progressively with the trough (Fig. 3a). On the right-hand side, the representation describes the offshore propagation of the trough for $x>12.5$ km. The discontinuity at $x=12.5$ km indicates the splitting point of the initial trough. In addition, the second discontinuity indicates the separation of the forced trough from the first system of waves. This separation occurs at $x=18$, 20, 22 and 32 km for different viscosities.

The curves of maximum heights show the formation of the main crest propagating in the slide direction ($x>13$ km), as well as the shoreward propagation of the second positive wave for $x<13$ km. This latter wave reflects at about $t=600$ s against the left side of the domain ($x=0$, at a water depth of 10 m), doubling its amplitude.

The main characteristic of Fig. 6(a) is the similarity of curves for $x<12$ km. From this figure it can be inferred that the influence of viscosity is weak for the shoreward-propagating system of waves and strong for the first dipole of waves propagating offshore. Numerical results show that the formation of the trough and of the second positive wave are directly linked to the geometry of the deforming mass, whose profiles are similar in the first instants ($t<90$ s), as shown in Fig. 6(b). The first dipole depends strongly on the landslide velocity and amplitudes are larger by a factor of 2 for a viscosity of 25 $m^2\ s^{-1}$ than for a viscosity of 500 $m^2\ s^{-1}$.

4.3 Water waves generated by granular flows

The Coulomb-type friction law is commonly used to model subaerial debris avalanches, considered as cohesionless granular avalanches (Savage & Hutter 1989; Hutter 1996). The same approximation may be used for submarine landslides, assuming that water plays a minor role for short run-out distances.

Sensitivity tests are carried out by varying the basal friction angle, φ, in the range determined by back-calculations from data sets of subaerial rock avalanches, i.e. from 7° to 17° (Voight 1979). In contrast to viscous flows that do not stop, granular flows reach a final position, which can be inferred from the friction angle. Numerical results show that the tangent of this angle is close to the slope of the line connecting the centres of gravity in the initial and final positions of the mass, suggesting that most of the initial potential energy is consumed by basal friction (Hutter 1996). The run-out distances of the landslide toe vary from 3–20 km (Fig. 7b) for elevation differences of 500–1200 m.

In contrast to viscosity, friction coefficients have a great influence on the second dipole of waves (Fig. 7a), which may be accounted for by the differences in the landslide profiles in the first instants ($t<90$ s) shown in Fig. 7(b). Similarly to viscous flows, the higher the landslide velocity (corresponding to small friction angles), the higher the first leading elevation wave and the initial trough (Fig. 7a).

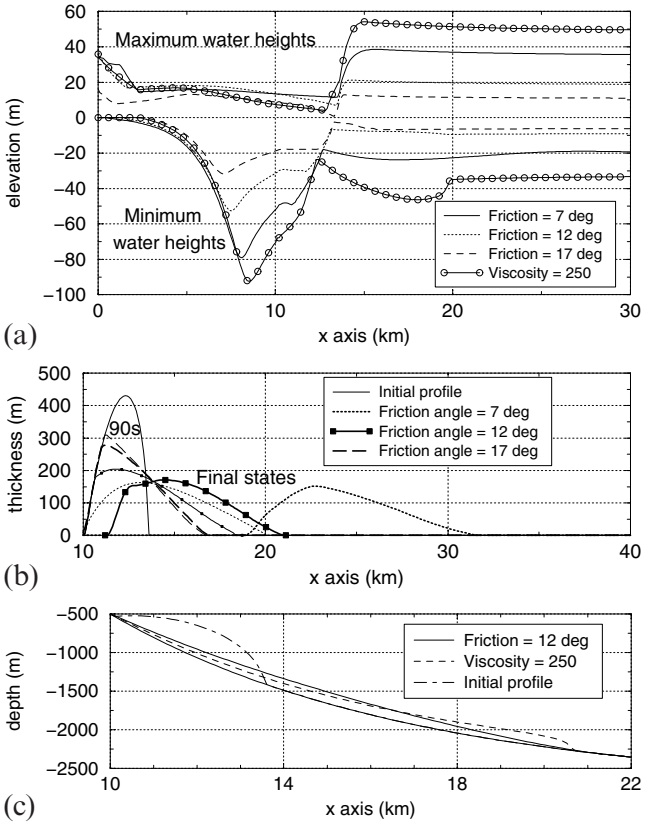

Figure 7. Influence of the basal friction on water wave generation by granular flow. Basal friction angles vary from $\varphi=7°$ to 17°. **(a)** Maximum and minimum water elevations reached during the tsunami propagation, stopped after reflection against the shoreline. **(b)** Comparisons between landslide profiles at $t=90$ s (thin lines) and in their final states (thick lines). **(c)** The represented domain is the grey-shaded area of Fig. 2. Comparison between profiles of a viscous flow ($\nu=250\ m^2\ s^{-1}$) and a granular flow ($\varphi=12°$) at $t=180$ s.

4.3.1 Formation of the second positive wave for different friction angles

For large values of the friction angle, the action of the landslide becomes negligible earlier. The second positive wave then forms earlier and unlike the other waves, its amplitude may be larger for higher frictions. Hence, a larger maximum height is observed for $\varphi=12°$ than for $\varphi=7°$ over the segment $3\ km<x<8$ km. This wave has a very steep front (Fig. 3b), so that further propagation in the shore direction is affected by non-linear effects and wave amplitudes converge to about the same value, about 15 m, before shoreline reflection.

The mechanics of landslides are complex and probably include both viscous and non-Newtonian rheologies, as has been proposed by several authors who used the simplified viscoplastic approach (Norem *et al.* 1991; McEwen & Malin 1989) described in Section 3.2. Numerical tests with $\varphi=7°$ and different viscosities show that combining viscosity and Coulomb-type friction slows down the landslide velocity without changing its geometry. The resulting maximum and minimum heights of the water surface are attenuated in the whole computed domain compared to water heights calculated with only basal friction.

4.4 Analysis of 1-D numerical results

The main aims of these simulations are (1) to validate the SW approach, (2) to determine the range of parameters of different friction laws, and (3) to compare and analyse their influence on landslide kinematics and on the water waves generated.

Fig. 7(a) shows a comparison of the maximum and minimum water heights calculated for granular flows and a viscous flow with $\nu = 250\ m^2\ s^{-1}$. The velocity of this landslide is similar during the first 90 s to that of the granular flow with $\varphi = 12^\circ$. For both flows, the maximum velocity is about $30\ m\ s^{-1}$ 1 min after landslide initiation. Fig. 7(a) shows that, for the same velocity, the viscous flow is much more efficient in producing high tsunami waves. The first leading elevation wave and the initial trough are higher by a factor of 2–3. This efficiency is mainly due to the larger mass concentration at the front of the landslide and the lesser thickness at the rear part (Fig. 7c). On the other hand, the amplitude of the second positive wave is larger for a Coulomb-type friction law from the generation area to a distance of 2 km off the coast. Further propagation is affected by non-linear effects (Figs 3a and b) and similar wave heights reach the coast.

The simulations show that the calculated water heights along the selected profile depend significantly on the constitutive laws that govern the landslide kinematics. Nevertheless, the comparison with observations can be made only at the shoreline, where run-up heights have been measured. Hence, the appropriate constitutive law cannot be inferred from a comparison at this single point for at least three reasons:

(1) the computed water heights at the shoreline are much higher than those observed due the absence of geometric dispersion that characterizes the 2-D propagation of real tsunamis;

(2) as a consequence, non-linear effects close to the coast affect tsunami propagation, and similar water heights of around 30 m are obtained at the shoreline for several friction laws;

(3) similar water heights at the shoreline may also be obtained for different constitutive laws by varying the volume or the depth of the landslide, which so far are not known with accuracy.

5 NUMERICAL SIMULATIONS OF THE PAPUA NEW GUINEA EVENT

The next section is devoted to 2-D simulations that will give a better constraint on landslide kinematics by comparing results with the run-up observations along a 40 km stretch of coast.

5.1 Description of the observed tsunami data

In the near field, post-tsunami surveys (Kawata *et al.* 1999a, 1999b) showed that run-up heights larger than 7.5 m were observed on a coastal segment of 20 km centred at Sissano lagoon (Fig. 8). Outside this segment, run-up heights decrease very rapidly, both eastwards and westwards, to benign values lower than 3–4 m. Inside this segment, strong variations of the measured run-up heights are observed, linked probably to the vegetation density in a flat region covered by a dense forest of pines and palm trees standing in the way of the tsunami. From these variations, it can be inferred that the highest run-up values are reached close to the shoreline in vegetation-dense regions, against which tsunami waves either splash or break or are reflected. This local tsunami is similar to the tsunamis of Nicaragua in 1992 (Imamura *et al.* 1993), Flores (Indonesia) in 1992 (Tsuji *et al.* 1995) and Peru in 1996 (Heinrich *et al.* 1998b), for which most of the reliable data are local maximum run-up heights. Since tsunami generation by landslides is a complex phenomenon, data inversion by backwards simulations is not investigated. Forward numerical simulations are carried out in a small domain covering an area of $80 \times 80\ km^2$, testing different landslides as tsunamigenic sources.

5.2 Qualitative description of tsunami simulations

Tsunami generation and propagation are simulated using the SW model tested in Section 4. As seen in 1-D simulations, tsunami simulation is based on the SW approximation, since frequency dispersion of waves may be neglected for short propagation distances. Moreover, run-up is not calculated, since the tsunami model uses a grid step of 100 m, which does not allow the introduction of a realistic friction coefficient on land taking into account the vegetation density. Our model, referred to in the literature as a threshold-type model, uses a minimum depth contour of 5 m and bottom friction is neglected everywhere. Complete reflection is calculated against the shoreline, which is the most realistic way of reproducing the largest observed heights. Nevertheless, preliminary simulations have shown that similar results are obtained when run-up is calculated using a large roughness coefficient on land (Chezy coefficient of the order of 1) in the first dry cells of the model. The distribution of calculated water heights is obtained by computing along the coast the maximum water surface elevation reached during tsunami propagation. It has been verified that the calculated distribution is almost identical when using a smaller grid size ($\Delta x = 50$ m) or threshold depths lower than 5 m.

As for the 1-D simulations on a simplified geometry, two systems of waves composed of one trough and one crest are generated by the landslide, one propagating mainly offshore and the other propagating shorewards. Nevertheless, these two systems of waves spread outwards from the source as cylindrical waves and reach the coast at different times with reduced amplitudes due to geometric dispersion (Figs 9a and b). The 20 km stretch centred at Sissano lagoon entrance is mainly affected by the second system of waves, i.e. the second positive wave, preceded by the leading trough. Beyond this segment, the coast is reached first by the first system of waves, i.e. the leading elevation wave, followed by the second system of waves. As already shown by Matsuyama *et al.* (1999), it is worth noting that the second positive wave does not spread out laterally due to energy focusing by a shallow shelf that extends offshore for 10 km from the Sissano region (Fig. 1).

5.3 Tsunami generated by a viscous flow

The first simulations have been carried out considering the landslide as a viscous flow with kinematic viscosity coefficients equal to 50, 150 and $500\ m^2\ s^{-1}$. As shown in Fig. 8, the smaller the viscosity, the larger the maximum height on each point of the coast, which leads to distinct curves of the calculated distribution. A comparison of the calculated and observed run-up height distributions shows two main discrepancies.

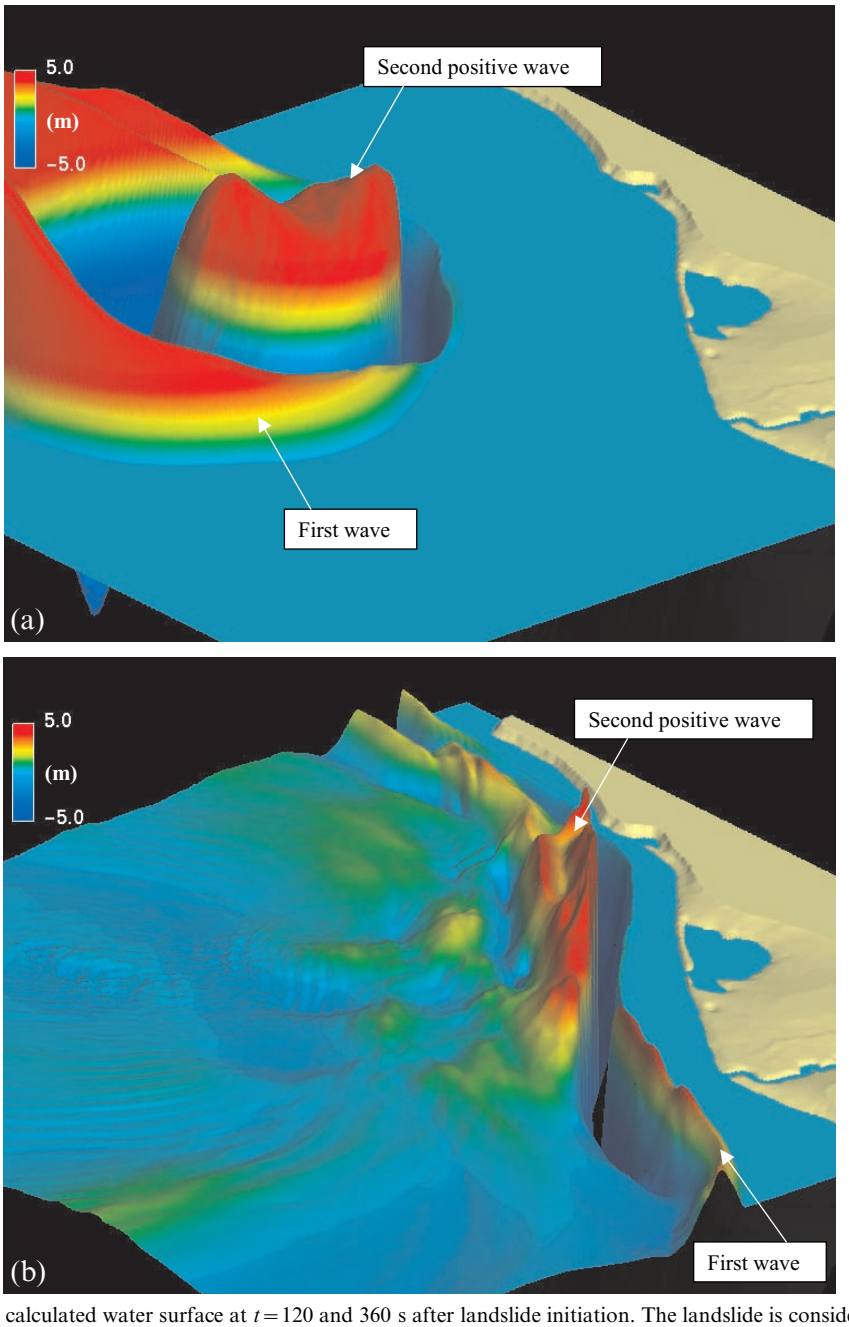

Figure 9. Snapshots of the calculated water surface at $t = 120$ and 360 s after landslide initiation. The landslide is considered as a viscous flow with $v = 50$ m^2 s^{-1}. Vertical scale is exaggerated by a factor 750 with respect to the horizontal dimensions (55 km by 55 km).

Outside the Sissano region ($x < 142^\circ$ and $x > 142.2^\circ$), maximum water heights range from 4 to 5 m in the western part and may exceed 10 m in the eastern part. In the western part, these large heights are attributed to the first leading elevation wave, refracted towards the coast. The second system of waves arrive about 3 min later but with smaller amplitudes. In the eastern part, both systems of waves produce higher amplitudes than those observed.

Inside the Sissano region, only the smallest viscosity value leads to maximum run-up heights around 15 m. A detailed analysis of water wave propagation from the generation area to Sissano shows that the second positive wave, whose front is very steep, is affected by energy dissipation due to non-linear effects when approaching the coast (Fig. 9b). Amplitudes of this wave decrease a few kilometres before the shoreline and tend towards values between 5 and 7 m above sea level before reflection at the shoreline.

5.4 Tsunami generated by a granular flow

In the second set of tests, the landslide is considered as a granular flow governed by a Coulomb-type friction law. Three constant friction angles are studied, 7°, 12° and 17°. As observed in 1-D sensitivity tests, the influence of basal friction on water heights in the direction of the coast is important, which leads to

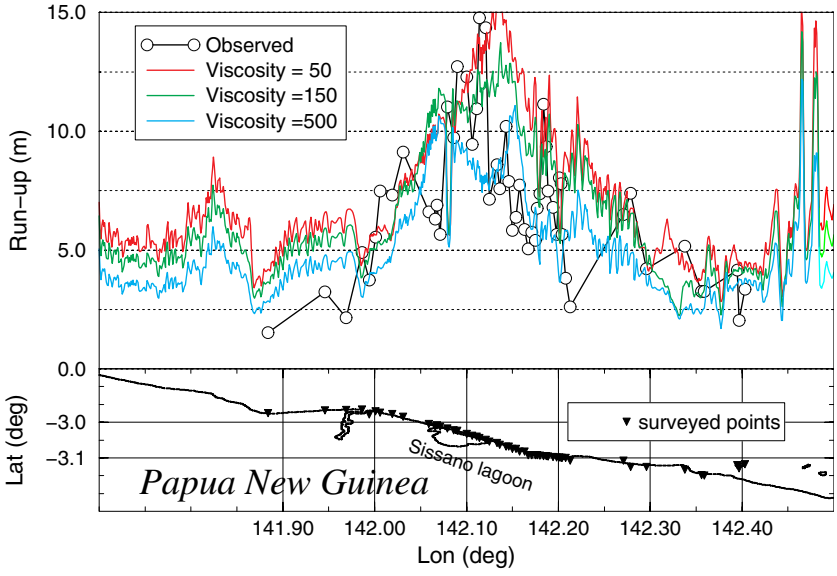

Figure 8. Comparison between observed run-up heights and calculated water heights for viscous flows with kinematic viscosities of 50, 150 and 500 $m^2\ s^{-1}$.

large differences of the calculated distribution (Fig. 10). In contrast to viscous flows, it is noted that the greater the friction, the narrower the distribution.

Comparisons between different friction angles show that the smaller the friction angle (corresponding to a higher slide velocity), the larger the first positive wave in the generation area. This wave remains higher when reaching the coast outside Sissano (Figs 11 and b), as observed for viscous flows. On the other hand, the second positive wave is attenuated in the generation area and later in the Sissano region. This attenuation is accounted for by a longer duration of the landslide, so that water sucking by the slide interferes with the filling in of the trough by surrounding water, that is, the formation of the second positive wave. The best fit to observations is obtained for $\varphi = 12°$, considering that the calculated water heights are those of reflected waves against the shoreline. In this case, the emplacement time for the leading edge of the landslide is slightly less than 2 min for a maximum vertical fall of about 500 m.

As for 1-D tests, the differences between the two constitutive laws may be accounted for by differences in mass distribution. In models of granular flows, mass distributions are much more uniform along the slope and thinner layers are produced at the front. In the generation area, water wave amplitudes are smaller by a factor of 2 for a non-Newtonian friction with $\varphi = 12°$ than for a viscous friction with $\nu = 150\ m^2\ s^{-1}$. When refracted towards the coast, both systems of waves are more energetic for viscous flows and amplitudes are higher approximately by a factor of 2 outside the 20 km stretch. On the other hand, the propagation from the source to the Sissano region is strongly affected by energy dissipation due to non-linear effects, since the front of the second positive wave is steeper for viscous flows than for granular flows.

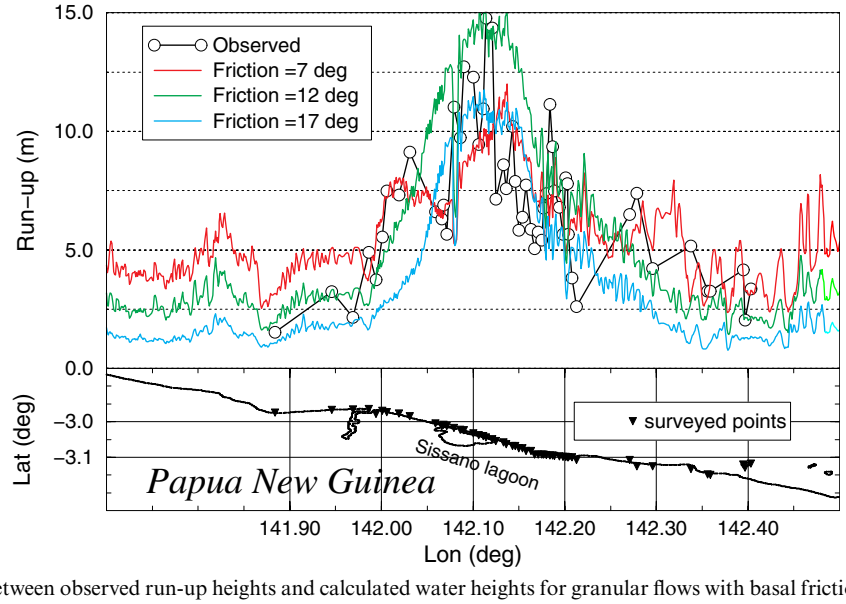

Figure 10. Comparison between observed run-up heights and calculated water heights for granular flows with basal friction angles of 7°, 12° and 17°.

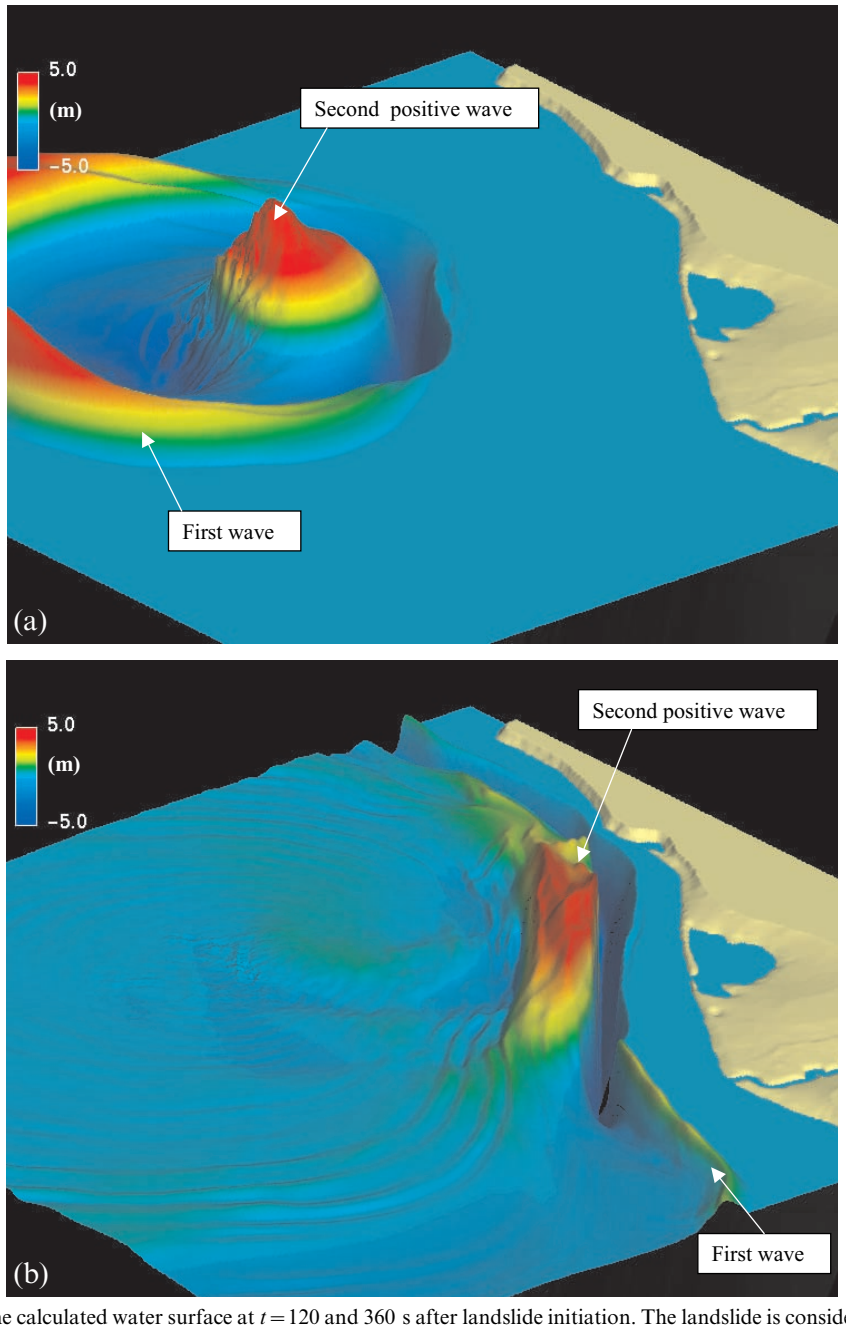

Figure 11. Snapshots of the calculated water surface at $t = 120$ and 360 s after landslide initiation. The landslide is considered as a granular flow with $\varphi = 12^\circ$. Same dimensions as in Fig. 9.

5.5 Influence of the water depth

The solution obtained in Section 5.4 is not unique, and sensitivity tests to the initial geometry have been carried out by varying the volume, the lateral position and the mean water depth of the landslide. Numerical results show that lateral variations of the landslide have a weak influence on the calculated water heights close to the coast. In contrast, water waves are sensitive to the mean depth of the landslide. Tests have been carried out for a deeper landslide and different friction angles. The top of the landslide is located at a depth of 800 m instead of 550 m, the geometry and the volume being similar. Numerical results, presented in Fig. 12 for two different friction angles $\varphi = 7^\circ$ and 12°, show that the distribution is qualitatively well reproduced but that the maximum water height, obtained for $\varphi = 12^\circ$, does not exceed 11.5 m. Numerical tests with larger volumes, with a similar geometry and located at the same water depth, show that volumes larger than 6 km^3 are required to reach water heights close to the observed ones inside the Sissano region. The maximum water height is 13 m for a volume of 6 km^3, sliding with a friction angle of 12° (Fig. 12).

5.6 Analysis of the simulations of the PNG event

The main results of the 2-D simulations are as follows.

(1) The observed run-up distribution is better reproduced for friction laws of non-Newtonian type than for Newtonian

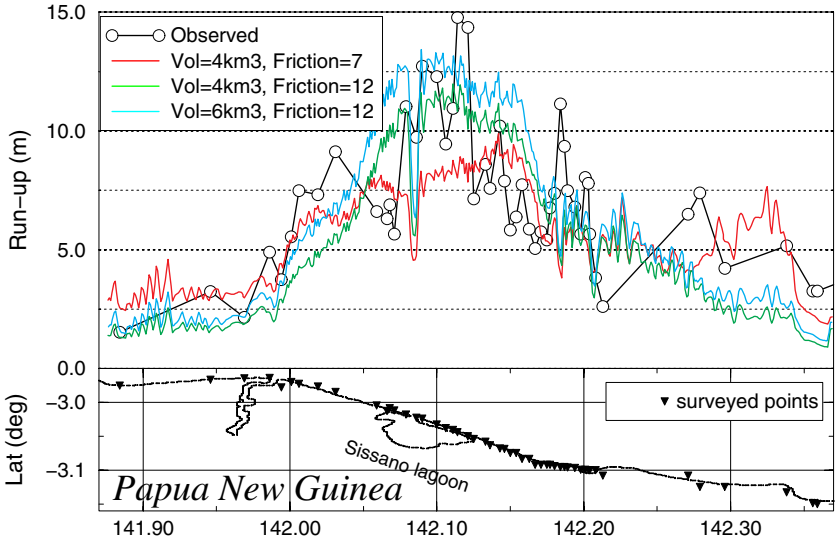

Figure 12. Influence of water depth and volume on water wave generation. The landslide is defined by an ellipsoidal shape, with its top located at 800 m instead of 550 m. Comparison between observed run-up heights and calculated water heights for a volume of 4 km^3 with basal friction angles of 7° and 12°, and for a volume of 6 km^3 with a basal friction angle of 12°.

laws. Viscous flows produce water height distributions along the coast flatter than those obtained for granular flows. The analysis of 1-D and 2-D simulations shows that the differences between water surfaces are due mainly to the thickness differences between the landslide fronts.

(2) The distribution of observed run-up heights has been reproduced numerically for a landslide with a volume of 4 km^3 located at water depths between 550 and 1500 m and sliding over a distance of 5 km with a Coulomb-type friction law. The associated basal friction angle is $\varphi = 12°$ in the range of friction angles determined for subaerial landslides. This friction angle controls the landslide run-out and allows the landslide toe to stop approximately at the observed location, that is, on a flat area at a water depth of 2000 m. The run-out distance is reduced to 2 km for a 17° friction angle and exceeds 20 km for friction angles lower than 7°.

There are two arguments against these conclusions.

(1) So far, the volume of the landslide and its initial position are not known with accuracy. The proposed solution is not unique and several combinations of landslide parameters might lead approximately to the same distribution of water heights. In particular, it has been shown in Section 5.5 that a similar distribution may be obtained for a landslide with a volume of 6 km^3 and with its top located initially at a water depth of 800 m.

(2) The numerical model we use is more appropriate for treating debris flows or debris avalanches than slumps composed of cohesive rocky material. Our model is inspired by the models of Jiang & Leblond (1992) and Fine *et al.* (1999), which have been applied to submarine landslides considered as viscous flows. In these models, the landslide is subject to gravity and friction and also to forces due to height gradients that are the origin of strong deformations. Other approaches could be tested in the early stages of the collapse such as the analytical model of Watts (1998), who considered a solid block motion, or the numerical model of Tinti *et al.* (1999), who considered the landslide as a rigid body consisting of blocks interacting with each other. The main feature of our model is considering the landslide as the flow of granular material following the approach of Savage & Hutter (1989). First, it is assumed that most deformations are concentrated at the bed surface, which is consistent with the preservation of pre-failure stratigraphy observed in landslide deposits. Second, we have introduced the possibility of basal friction of Coulomb-type, which allows the landslide to stop. It is worth noting that the limited run-out of this landslide, of the order of a few kilometres, is reproduced by our simulation.

6 CONCLUSIONS

The efficiency of deep submarine landslides in producing tsunamis has been studied by means of numerical models, with application to the 1998 Papua New Guinea event. Preliminary 1-D simulations of this event on a simplified geometry have allowed us to validate the SW approach, to study the influence of different friction laws governing the landslide motion and to define the associated rheological parameters.

Based on these parameters, 2-D simulations of the 1998 Papua New Guinea event have been carried out and have shown that the distribution of observed run-up heights could be reproduced for a landslide of 4 km^3 located 20 km offshore and sliding with a non-Newtonian friction law and a basal friction coefficient of $\varphi = 12°$. As shown by numerical computations and considering the data uncertainties, this set of landslide parameters is not unique. The main result of 2-D simulations is to confirm that the tsunami is likely to be due to a deep and large submarine landslide. The fact that it was triggered by a relatively moderate earthquake suggests that coastal areas with large sediment deposits are at significant risk and precise surveying of such structures is warranted (Synolakis *et al.* 1997).

ACKNOWLEDGMENTS

We are grateful to R. Roche for fruitful discussions concerning numerical schemes, D. Tappin, Ph. Watts and SOPAC Institute for providing bathymetric data and estimates of the landslide geometry, and E. Okal for scientific discussions concerning the PNG seismic event.

REFERENCES

Alcrudo, F. & Garcia-Navarro, P., 1993. A high-resolution Godunov-type scheme in finite volumes for the 2D shallow water equations, *Int. J. Num. Meth. Fluids,* **16,** 489–505.

Assier, S., Mariotti, C. & Heinrich, Ph., 1997. Numerical simulation of submarine landslides and their hydraulic effects, *J. Waterway Port Coast. Oc. Eng.,* **123,** 149–157.

Bagnold, R., 1954. Experiments on a gravity-free dispersion of large solid particles in a Newtonian fluid under shear, *Proc. R. Soc. Lond.,* **A225,** 49–63.

Dade, W. & Huppert, H., 1998. Long run-out rockfalls, *Geology,* **26,** 803–806.

Douady, S., Andreotti, B. & Daerr, A., 1999. On granular surface flow equations, *Eur. Phys. J. B,* **11,** 131–142.

Fine, I., Rabinovich, A., Kulikov, E., Thomson, R. & Bornhold, B., 1999. Numerical modelling of landslide-generated tsunamis with application to the Skagway harbor tsunami of November 3, 1994, in *Int. Conf. on Tsunamis, Paris, France, May 26–28, 1998,* pp. 211–233, Publ. CEA/DASE, Bruyeres-le-Chatel, France.

Fraccarollo, L. & Toro, E., 1995. Experimental and numerical assessment of the shallow water model for two-dimensional dam-break type problems, *J. hydr. Res.,* **33,** 843–864.

Hampton, M., Lee, H. & Locat, J., 1996. Submarine landslides, *Rev. Geophys.,* **34,** 33–59.

Harbitz, C., 1992. Model simulations of tsunamis generated by the Storegga slides, *Mar. Geol.,* **105,** 1–21.

Harten, A., 1983. High resolution scheme for hyperbolic conservation laws, *J. Comput. Phys.,* **49,** 357–393.

Heinrich, Ph., 1992. Nonlinear water waves generated by submarine and aerial landslides, *J. Waterway Port Coast. Oc. Eng.,* **118,** 249–266.

Heinrich, Ph., Mangeney, A., Guibourg, S., Rocher, R., Boudon, G. & Cheminee, J.L., 1998a. Simulation of water waves generated by a potential debris avalanche in Montserrat, Lesser Antilles, *Geophys. Res. Lett.,* **25,** 3697–3700.

Heinrich, Ph., Schindele, F., Guibourg, S. & Ihmle, P., 1998b. Modeling of the February 1996 Peruvian tsunami, *Geophys. Res. Lett.,* **25,** 2687–2690.

Heinrich, Ph., Piatanesi, A., Okal, E. & Hébert, H., 2000. Near-field modeling of the July 17, 1998 tsunami in Papua New Guinea, *Geophys. Res. Lett.,* **27,** 3037–3040.

Hutter, K., 1996. Avalanche dynamics, a review, in *Hydrology of Disasters,* pp. 317–394, ed. Singh, V.P., Kluwer, Amsterdam.

Imamura, F., Shuto, N., Ide, S., Yoshida, Y. & Abe, K., 1993. Estimate of the tsunami source of the 1992 Nicaraguan earthquake from tsunami data, *Geophys. Res. Lett.,* **20,** 1515–1518.

Iverson, R., 1997. The physics of debris flows, *Rev. Geophys.,* **35,** 245–296.

Iwabuchi, Y., Satake, K., Nakamura, M., Matsumoto, T. & Matsumoto, Y., 2000. Bathymetry of the source region of 1998 Papua New Guinea tsunami, *EOS, Trans. Am. geophys. Un.,* **81,** 22 (abstract).

Jiang, L. & Leblond, P., 1992. The coupling of a submarine slide and the surface waves which it generates, *J. geophys. Res.,* **97,** 731–744.

Jiang, L. & Leblond, P., 1993. Numerical modeling of an underwater Bingham plastic mudslide and the waves which it generates, *J. geophys. Res.,* **98,** 304–317.

Kajiura, K., 1963. The leading wave of a tsunami, *Bull. earthq. Res. Inst.,* **41,** 535–571.

Kanamori, H., 1972. Mechanism of tsunami earthquakes, *Phys. Earth planet. Inter.,* **6,** 346–359.

Kawata, Y.B. *et al.*, 1999a. Tsunami in Papua New Guinea was as intense as first thought, *EOS, Trans. Am. geophys. Un.,* **80,** 104–105.

Kawata, Y.B. *et al.*, 1999b. Field survey on the 1998 tsunami in the northwestern area of Papua New Guinea, in *Rept for Grant-in-Aid for Scientific Research, Ministry of Education, Science, Sports and Culture, Japan,* pp. 1–81, DPRI, Kyoto University.

Kikuchi, M., Yamanaka, Y., Abe, K., Morita, Y. & Watada, S., 1998. Source rupture process of the Papua New Guinea Earthquake of July 17, 1998 inferred from teleseismic body waves, *EOS, Trans. Am. geophys. Un.,* **79,** 45 (abstract).

Kilburn, C. & Sorensen, S., 1998. Runout lengths of sturzstroms: the control of initial conditions and of fragment dynamics, *J. geophys. Res.,* **103,** 17 877–17 884.

Laigle, D. & Coussot, Ph., 1997. Numerical modeling of mudflows, *J. hydraul. Eng.,* **123,** 617–623.

Mangeney, A., Heinrich, Ph. & Roche, R., 2000. Analytical and numerical solution of dam-break problem for application to water floods, debris and dense snow avalanches, *Pure appl. Geophys.,* **157,** 1081–1096.

Matsuyama, M., Walsh, J. & Yeh, H., 1999. The effect of bathymetry on tsunami characteristics at Sissano lagoon, Papua New Guinea, *Geophys. Res. Lett.,* **26,** 3513–3516.

McEwen, A. & Malin, M., 1989. Dynamics of Mount St Helens' 1980 pyroclastic flows, rockslide-avalanche, lahars and blast, *J. Volc. Geotherm. Res.,* **37,** 205–231.

Moore, J., Clague, D., Holcomb, R., Lipman, P., Normark, W. & Torresan, M., 1989. Prodigious submarine landslides on the Hawaiian Ridge, *J. geophys. Res.,* **94,** 17 645–17 684.

Naaim, M., Vial, S. & Couture, R., 1997. Saint-Venant approach for rock avalanches modelling, *Saint-Venant Symp.,* Paris.

Newman, A. & Okal, E., 1998. Teleseismic estimates of radiated seismic energy: the E/M_0 discriminant for tsunami earthquakes, *J. geophys. Res.,* **103,** 26 885–26 898.

Nomanbhoy, N. & Satake, K., 1995. Generation mechanism of tsunamis from the 1883 Krakatau eruption, *Geophys. Res. Lett.,* **22,** 509–512.

Norem, H., Locat, J. & Schieldrop, B., 1991. An approach to the physics and the modelling of submarine flowslides, *Mar. Geotech.,* **9,** 93–111.

Okal, E., 1999a. The 1998 Papua New Guinea tsunami: an overview, in *Int. Conf. on Tsunamis, Paris, France, May 26–28, 1998,* pp. 111–116, Publ. CEA/DASE, Bruyeres–le–Chatel, France.

Okal, E., 1999b. The probable source of the 1998 Papua New Guinea tsunami as expressed in oceanic T waves, *EOS. Trans. Am. geophys. Un.,* **80,** 46 (abstract).

Pelinovsky, E. & Poplavsky, A., 1996. Simplified model of tsunami generation by submarine landslides, *Phys. Chem. Earth,* **21,** 13–17.

Pouliquen, O., 1999. Scaling laws in granular flows down rough inclined planes, *Phys. Fluids,* **11,** 542–548.

Rabinovich, A., Thomson, R., Kulikov, E., Bornhold, B. & Fine, I., 1999. The landslide-generated tsunami of November 3, 1994 in Skagway harbor, Alaska, a case study, *Geophys. Res. Lett.,* **26,** 3009–3012.

Sander, J. & Hutter, K., 1992. Evolution of weakly non-linear channelized shallow water waves generated by a moving boundary, *Acta Mech.,* **91,** 119–155.

Sander, J. & Hutter, K., 1996. Experimental and computational study of channelized water waves generated by a porous body, *Acta Mech.,* **115,** 133–149.

Savage, S. & Hutter, K., 1989. The motion of a finite mass of granular material down a rough incline, *J. Fluid Mech.,* **199,** 177–215.

Savage, S. & Hutter, K., 1991. The dynamics of avalanches of granular materials from initiation to runout, Part I: analysis, *Acta Mech.,* **86,** 201–223.

Sousa, J. & Voight, B., 1991. Continuum simulation of flow failures, *Geotechnique,* **41,** 515–538.

Sousa, J. & Voight, B., 1995. Multiple pulsed debris avalanche emplacement at Mount St, Helens in 1980: Evidence from numerical continuum flow simulations, *J. Volc. Geotherm. Res.,* **66,** 227–250.

Sweet, S., Silver, E., Davies, H., Matsumoto, T., Watts, P. & Synolakis, C.E., 1999. Seismic reflection images of the source region of the Papua New Guinea tsunami of July 17, 1998, *EOS. Trans. Am. geophys. Un.,* **80,** 46 (abstract).

Synolakis, C., Liu, P., Carrier, G. & Yeh, H., 1997. Tsunamigenic sea-floor deformations, *Science,* **278,** 598–600.
Tanioka, Y., 1999. Analysis of the far-field tsunamis generated by the 1998 Papua New Guinea earthquake, *Geophys. Res. Lett.,* **26,** 3393–3396.
Tappin, D.R. *et al.*, 1999a. Sediment slump likely caused 1998 Papua New Guinea tsunami, *EOS. Trans. Am. geophys. Un.,* **80,** 329, 334, 340.
Tappin, D.R., Watts, P., Borrero, J., Okal, E., Bardet, J.-P., Grilli, S., Matsumoto, T. & Synolakis, C.E., 1999b. Submarine slump generation of the 1998 Papua New Guinea tsunami: the evidence so far, *EOS. Trans. Am. geophys. Un.,* **80,** 46 (abstract).
Tinti, S. & Bortolucci, E., 2000. Analytical investigation on tsunamis generated by submarine landslides, *Ann. Geofis.,* **43,** 519–536.
Tinti, S., Bortolucci, E. & Vannini, C., 1997. A block-based theoretical model suited to gravitational sliding, *Natural Hazards,* **16,** 1–28.
Tinti, S., Bortolucci, E. & Armigliato, A., 1999. Numerical simulation of the landslide-induced tsunami of 1988 in Vulcano island, Italy, *Bull. Volcanol.,* **61,** 121–137.
Titov, V. & Gonzalez, F., 1998. Numerical study of the source of the July 1998 PNG earthquake, *EOS. Trans. Am. geophys. Un.,* **79,** F572 (abstract).
Titov, V. & Gonzalez, F., 2000. Numerical study of the source of the 17 July 1998 PNG tsunami, *EOS. Trans. Am. geophys. Un.,* **81,** 22 (abstract).
Titov, V. & Synolakis, C., 1998. Numerical modeling of tidal wave runup, *J. Waterways Port Coast. Oc. Eng.,* **124,** 157–170.
Torrey, M., Mjolsness, R. & Stein, L., 1987. Nasa-Vof3D: a three-dimensional computer program for incompressible flows with free surfaces, *Rept LA11009-MS,* Los Alamos National Laboratory.
Tsuji, Y. *et al.*, 1995. Damage to coastal villages due to the 1992 Flores Island earthquake tsunami, *Pure appl. Geophys.,* **144,** 481–524.
Van Leer, B., 1979. Toward the ultimate conservation difference scheme V. A second order sequel to Godunov's method, *J. Comput. Phys.,* **32,** 101–136.
Voight, B., 1979. *Rockslides and Avalanches, 2, Engineering Sites, Developments in Geotechnical Engineering,* Vol. 14b, Elsevier, Amsterdam.
Watts, P., 1998. Wavemaker curves for tsunamis generated by underwater landslides, *J. Waterways Port Coast. Oc. Eng.,* **124,** 127–137.

APPENDIX A: THE NAVIER–STOKES MODEL

The NS model is based on the 3-D hydrodynamics code of Torrey *et al.* (1987) developed for a single fluid. It solves the NS equations with a free surface for a mixture of two incompressible fluids using an Eulerian finite difference method. The 2-D version of this numerical model has been validated by laboratory experiments consisting of the submarine sliding of a gravel mass along an inclined plane (Assier *et al.* 1997). The main characteristic of such a model is that it deals with only one fluid with variable density in time and space. The mixture is composed here of sea water, taken as a fluid of density $\rho_w = 1$, and the debris material, treated as a homogeneous fluid of density $\rho_s = 2$. The mixture density ρ is defined by the relation $[\rho = (1-c)\rho_w + c\rho_s]$, where c is the volume fraction of sediments. The non-linear governing equations for the mixture can then be written as follows:

$$\frac{\partial \rho}{\partial t} + \nabla \cdot (\rho \mathbf{v}) = 0 \qquad \text{(continuity equation)},$$

$$\frac{\partial \mathbf{v}}{\partial t} + \mathbf{v} \cdot \nabla \mathbf{v} = \mathbf{g} - \frac{\nabla p}{\rho} + \nabla \cdot \boldsymbol{\tau} \qquad \text{(momentum equation)},$$

$$\frac{\partial F}{\partial t} + \nabla \cdot F\mathbf{v} = 0 \qquad \text{(transport equation)},$$

$$\nabla \cdot \mathbf{v} = \frac{\rho_s - \rho_w}{\rho_s \rho_w} \nabla \cdot \mathbf{j} \qquad \text{(diffusion equation)},$$

where $\mathbf{v}$ is the 3-D fluid velocity vector of the mixture, $\mathbf{g}$ is the acceleration due to gravity, p is the pressure, $\mathbf{j}$ is the diffusion flux and is set at 0, since no dilution of debris material into water is calculated, and F is the fractional volume of the cell occupied by the mixture and is used to calculate the free-surface evolution. The model being Eulerian, the resolution of the continuity equation leads to the classical problem of numerical diffusion at the interface between water and sediments. To suppress this, a method based on a donor-acceptor technique has been developed to determine the interface.

The computational domain in this study extends over 50 km in the x-direction and from -3000 m to 100 m in the vertical direction. The mesh consists of 500 cells in the horizontal directions and 200 cells in the vertical direction. The minimum horizontal grid increment is 50 m in the generation area and the vertical grid increment is 5 m at the water surface and increases progressively upwards and down to the bottom. The landslide is modelled at $t = 0$ s by approximately 900 cells.